Article

Process Optimization of In Situ Magnetic-Anisotropy Spark Plasma Sintering of M-Type-Based Barium Hexaferrite $BaFe_{12}O_{19}$

Haetham G. Mohammed [1], Thar Mohammed Badri Albarody [1,*], Susilawati Susilawati [2,3,*], Soheil Gohari [4], Aris Doyan [2,3], Saiful Prayogi [5], Muhammad Roil Bilad [5], Reza Alebrahim [6] and Anwar Ameen Hezam Saeed [7]

1   Department of Mechanical Engineering, Universiti Teknologi Petronas, Seri Iskandar 32610, Malaysia; haetham_19000233@utp.edu.my
2   Master of Science Education Program, University of Mataram, Mataram 83125, Indonesia; aris_doyan@unram.ac.id
3   Physics Education, FKIP, University of Mataram, Mataram 83125, Indonesia
4   Department of Mechanical Engineering, The University of Melbourne, Parkville, VIC 3010, Australia; soheil.gohari@unimelb.edu.au
5   Faculty of Applied Science and Enginering, Universitas Pendidikan Mandalika, Mataram 83126, Indonesia; saifulprayogi@ikipmataram.ac.id (S.P.); muhammadroilbilad@ikipmataram.ac.id (M.R.B.)
6   Industrial Engineering Department, University of Padova, 35131 Padova, Italy; reza.alebrahim@unipd.it
7   Department of Chemical Engineering, Universiti Teknologi Petronas, Seri Iskandar 32610, Malaysia; anwar_17006829@utp.edu.my
*   Correspondence: dher.albarody@utp.edu.my (T.M.B.A.); susilawatihambali@unram.ac.id (S.S.); Tel.: +60-1128480693 (T.M.B.A.)

Abstract: This paper introduces a new spark plasma sintering technique that is able to order crystalline anisotropy by in-series/in situ DC electric coupled magnetic field. The process control parameters have been investigated on the production of anisotropic $BaFe_{12}O_{19}$ magnets based on resulted remanence (Mr). Sintering holding time (H.T.), cooling rate (C.R.), pressure (P), and sintering temperature (S.T.) are optimized by Taguchi with L9 orthogonal array (OA). The remanent magnetization of nanocrystalline $BaFe_{12}O_{19}$ in parallel ($Mr^{\parallel}$) perpendicular ($Mr^{\perp}$) to the applied magnetic field was regarded as a measure of performance. The Taguchi study calculated optimum process parameters, which significantly improved the sintering process based on the confirmation tests of $BaFe_{12}O_{19}$ anisotropy. The magnetic properties in terms of $Mr^{\parallel}$ and $Mr^{\perp}$ were greatly affected by sintering temperature and pressure according to ANOVA results. In addition, regression models were developed for predicting the $Mr^{\parallel}$ as well as $Mr^{\perp}$ respectively.

Keywords: spark plasma sintering; sintering parameters; remanence; optimization; magnet; magnetic properties; anisotropic magnet

1. Introduction

Barium hexaferrite ($BaFe_{12}O_{19}$) has been one of the most widely used magnetic materials, accounting for nearly 90% of the $4 billion global market due to its superior properties such as low manufacturing costs, high Curie temperature, high coercivity, chemical stability, and corrosion resistance [1–5]. The production of hexagonal $BaFe_{12}O_{19}$ has reached 300,000 tons annually, equivalent to 50 g per person [2,6–9]. Due to its hexagonal structure, the material was called barium hexaferrite. The structure is magnetoplumbite/M-type with the general formula of $MFe_{12}O_{19}$ or $MO_{0.6}Fe_2O_3$, in which M can be barium (Ba), strontium (Sr), or lead (Pb) [10].

In the last few decades, numerous techniques, such as the co-precipitation method [11], the sol-gel method [12], the hydrothermal/solvothermal method [13], and the solid-state method [14] have been developed to synthesize this barium-based hexaferrite $BaFe_{12}O_{19}$.

Growing annealing temperature is frequently needed to obtain a pure phase of $BaFe_{12}O_{19}$, which deteriorates the magnetic properties. Barium hexaferrite single crystals have received a lot of attention in the last decade because of their high saturation magnetization and large magneto-crystalline anisotropy along the crystallographic c-axis [15], but due to their high-temperature melting point, synthesizing these single crystals is a very expensive and difficult task. A textured hexaferrite with high performance is seen as a good alternative since they have properties that are comparable to single-crystal hexaferrite [16].

In order to take advantage of the strong magnetic properties imparted by the magnetic uniaxial anisotropy, the M-type hexaferrite particles must be oriented along the c-axis of the crystal direction, which corresponds to a magnetically easy-axis and perpendicular to the hexagonal platelet-shaped plane [17].

Textured ceramics have been developed using a variety of processing techniques, including tape casting [18], multilayer screen printing [19], hot forging [20], and grain growth [21]. Synthesis of textured hexaferrite has previously been shown to be a time-consuming process that often necessitates special processing conditions such as a strong external magnetic field during the processing.

In contrast to traditional sintering methods such as hot press (HP) or hot isostatic press (HP), spark plasma sintering (SPS) is a relatively new sintering process for the densification of various ceramic or metallic systems at a low sintering temperature and a very short sintering time [22–27]. SPS-compacted M-type barium-based hexaferrite bulk magnets have previously been published, but all samples showed only magnetically isotropic behavior [28–31]. Anisotropic barium hexaferrite is produced by adding NaCl salt during the sintering process at low sintering temperature. The addition of NaCl to the powder during the sintering process has proven to be an effective way in the alignment of particles along the magnetic easy-axis, but this method is limited to a certain low sintering temperature and also to a lengthy time-consumption [32]. So far, some permanent magnets coupled with SPS have been used in the alignment of sintered powders such as Sm-Co magnet with Curie temperature of 800 °C which was utilized during the sintering of Sm–Fe–N [33]; as well as Halbach magnet with a uniaxial magnetic field of 1T, which was used to assist spark plasma sintering of $Co_{80}Ni_{20}$ nanowires [34]; also two commercial Sm_2Co_{17} bulk magnets (mμ0Br ≈1.10 T at 300 K, max working temperature (≈300 °C), which were utilized to assist anisotropic SPS-compacted MnBi magnets [35]. From the results obtained, the sintered magnets had high densities with anisotropic behavior and the external magnetic fields contributed to the enhancement of the Mr/Ms ratios of SPS-compacted samples, as in Figure 1.
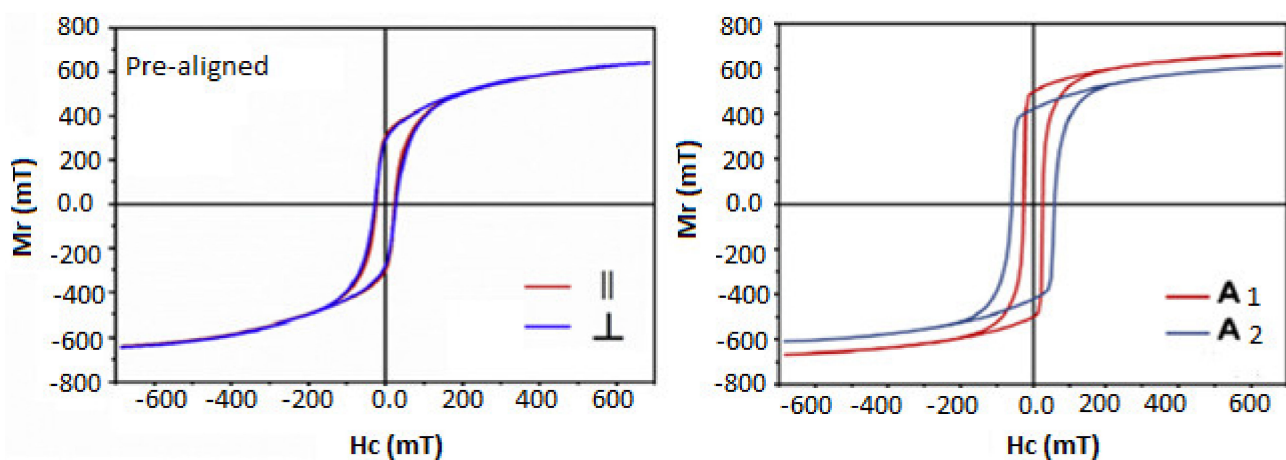

Figure 1. $M^{\parallel}$ (H) curves for the in situ aligned samples without binder during the SPS process, adopted from Ref. [35].

The process parameters of spark plasma sintering, such as holding time, cooling rate, sintering temperature, pressure, and heating rate directly affect the mechanical, magnetic,

and electrical properties of sintered materials. However, when the holding temperature is reached quickly during spark plasma sintering, compaction occurs with minimal grain growth. This phenomenon has been investigated using a variety of ceramic and metallic materials to create a full-densification nanostructure sample [25,36,37]. The sintering temperature increases in crystal size and density. In contrast, the heating rate had the opposite effect [38]. The density of sintered materials is affected by holding time, whereas, with the increase in holding time, the density of sintered boron carbide and Si_3N_4-SiC increased [39,40].

Indeed, the design of experiment (DOE) model emerged recently as a statistical method providing solutions for simplifying the manufacturing process of materials, optimizing process parameters, and minimizing unwanted trial by error approach. Therefore, the DOE approach helps to standardize production processes, reduce operational cost, minimize wastage, saves energy, saves time, and ensures accurate results in experimental studies [41]. In the 1920s, RA Fisher from England introduced the design of experiment (DOE) as a statistical tool used in studying the effect of multiple variables. However, the Taguchi method originated as the standard version of DOE by Dr. Genechi Taguchi, which was the most economically-friendly method used for experimental design [42]. Taguchi employs orthogonal arrays (OA), which are constructed so that the controllable variables can be analyzed with their respective responses at different levels in an ordered manner resulting in the smallest number of experiments, thus saving money and time. Limited studies have been reported in the literature in optimizing the spark plasma sintering. Moreover, Velmurugan et al. [43] used response surface methodology (RSM) to optimize SPS parameters such as temperature, holding time, and pressure for Si_3N_4-SiC/$MgSiN_2$ composite. The optimized parameters enhanced the mechanical properties such as hardness and fracture toughness. Moreover, Ujah et al. [42] used Taguchi design in the experiment in their study on the optimization of SPS parameters of Al-CNTs-Nb nano-composite, where the sintering temperature, pressure, heating rate, and holding time were optimized. There was close agreement between DOE results (Taguchi predicted result) and experimental results (density and hardness).

As mentioned above, all previous researches focusing on the influence of the external magnetic field during the sintering process were restricted to permanent magnet usage with limited Curie temperature. There was also a lack of studies and analysis on the effect of various sintering parameters on the magnetic properties of soft and hard magnetic nanopowders during the sintering process.

This work introduces new spark plasma sintering (SPS) technique with magnetic anisotropy for magnetite ceramic sintering and grains alignment control to enhance the magnetic properties. Anisotropy of sintered barium ferrite $BaFe_{12}O_{19}$ is used to validate the SPS processing parameters that were optimized by (L9) Taguchi design of experiment (DOE) with (ANOVA) statistical tool. Furthermore, predictive magnetic remanence $Mr^{\parallel}$ and $Mr^{\perp}$ models were developed using regression analysis.

2. Materials and Methods

2.1. Materials

Nanocrystallites of M-type barium hexaferrite ($BaFe_{12}O_{19}$) powder with 100 nm average particle size (99% purity) was purchased from (Sigma-Aldrich (M) Sdn Bhd, Selangor D.E, Malaysia), and used as a starting material for this study.

2.2. Magnetic Anisotropic Spark Plasma Sintering (MASPS)

A spiral magnetic coil with a rectangular cross-section, isolated by fiberglass and circular water pipes, is directly connected to the SPS's cathode and anode (two spacers). This magnetic coil is designed to work coupled with SPS to generate a magnetic field in the same direction of electrical current, as shown in Figure 2. Table 1 presents the magnetic field generated from the coil at different sintering temperatures.
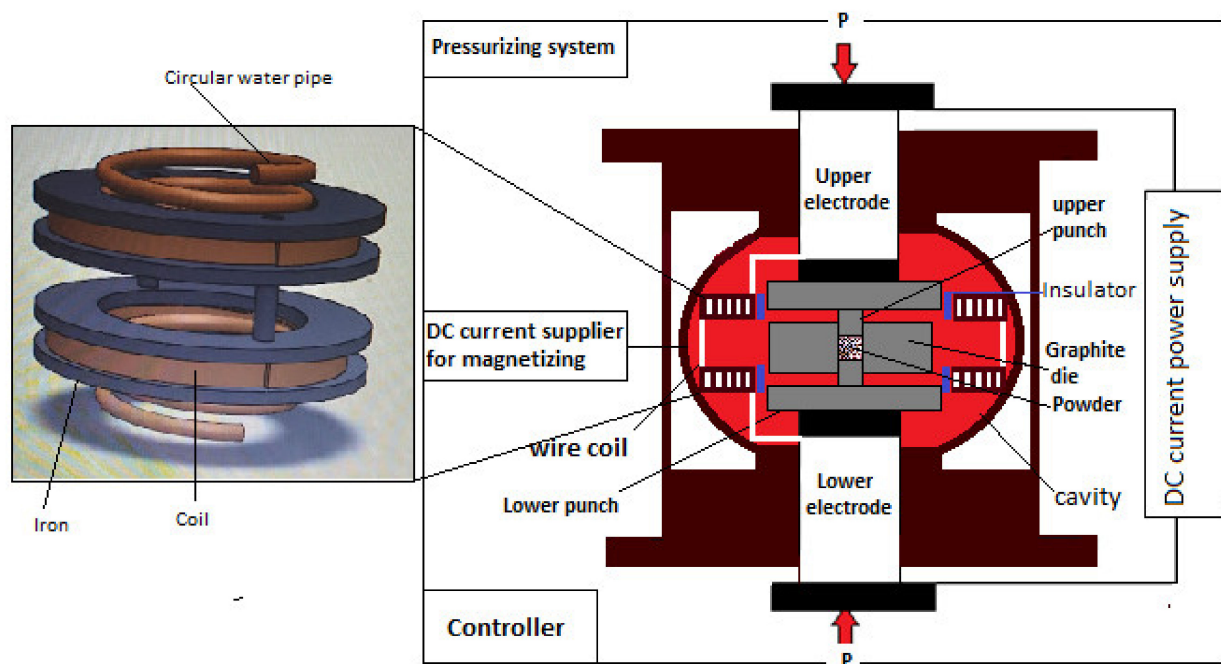
Figure 2. Schematic diagram of magnetic-anisotropic spark plasma sintering (MASPS).

Table 1. Magnetic field (mT) to current (A) relation.

NO	Current (A)	Temperature (°C)	Magnetic Field (mT)
1	150	650	40
2	200	780	44
3	250	920	70
4	300	1050	80
5	350	1180	90

2.3. Sintering Parameters

The sintering process is mainly affected by different parameters. In this study, the effect of holding time (H.T.), cooling rate (C.R.), pressure (P), and sintering temperature (S.T.) on the magnetic properties of nanopowder are studied experimentally using a developed magnetically-assisted spark plasma sintering method. Table 2 shows the parameters and their levels used in this study, while the heating rate is used as a fixed parameter at 100 °C/min.

Table 2. Sintering process parameters and their levels.

Symbols	Process Parameters	Unit	Levels		
			1	2	3
H.T.	Holding time	S	60	120	180
C.R.	Cooling rate	°C/min	50	150	250
P	Pressure	MPa	30	45	60
S.T.	Sintering temperature	°C	920	1050	1180

2.4. Design of Experiment (DOE)

Recently, DOE is considered as a statistical tool that employs the Taguchi orthogonal arrays (OA), so that the controllable variables can be analyzed with their respective responses at different levels in an ordered manner, which leads to the reduction of the number of experiments, thus saving money and time. However, by applying the Taguchi

method, a system with three levels and four factors (parameters) L9 is the most suitable orthogonal array (OA) used as a DOE tool parameter in the experimental works.

A Minitab 17.0 (2017) software (Minitab LLC, State College, PA, USA) is used to input and analyze the sintering data. Based on the randomized OA, a total of 9 runs of experiments were conducted on MASPS in the order from trial 1 to trial 9. The experimental data for sintering process tests are shown in Table 3.

Table 3. Experimental data for the sintering process.

Run	Holding Time (min)	Cooling Rate (°C/min)	Pressure (MPa)	Sintering Temperature (°C)
1	60	50	30	920
2	60	100	45	1050
3	60	150	60	1180
4	120	50	45	1180
5	120	100	60	920
6	120	150	30	1050
7	180	50	60	1050
8	180	100	30	1180
9	180	150	45	920

2.5. Experimental Process

$BaFe_{12}O_{19}$ powder was heated at 100 °C for 1 h to remove the moisture using a tube furnace under the Argon atmosphere. After the powder was cooled, it was taken out for weighing. Then, 0.4 ± 0.001 g of the powder was weighed using a digital balance. the powder was manually placed into a graphite mold, where the inner diameter of the graphite sleeve is 10 mm. The graphite mold consists of two 10 mm punches in diameter and a sleeve. The lower punch was inserted into the sleeve before the powder was poured into the sleeve. To avoid adhering to the interior of the mold and the punches, powders were separated by 0.1 mm graphite foils. The graphite mold with $BaFe_{12}O_{19}$ was then placed between two graphite spacers to compact the powder under specified pressures (DOE).

The sintering temperature, holding time, and cooling rate were specified by following the DOE, as shown in Table 4. Additionally, the surface temperature of the graphite sleeve was measured using IR thermometer sensor, where PID was utilized to monitor the sintering process. The heating rate is fixed at 100 °C/min. Manually, a gaussmeter was used to measure the generated magnetic field of the magnetic coil at the sintering temperature.

Table 4. The results of experiments and the calculated S/N ratio.

Exp. Runs	Results		S/N Ratio of Results	
	$Mr^{\parallel}$ (emu/g)	$Mr^{\perp}$ (emu/g)	$Mr^{\parallel}$ (dB)	$Mr^{\perp}$ (dB)
1	22.70	10.89	27.12	−20.74
2	20.30	9.50	26.14	−19.55
3	20.80	9.78	26.36	−19.80
4	22.00	10.60	26.84	−20.50
5	16.00	7.00	24.08	−16.90
6	19.80	9.20	25.93	−19.27
7	17.66	8.00	24.93	−18.06
8	22.00	10.60	26.84	−20.50
9	16.00	7.00	24.08	−16.90

2.6. Sample Preparation and Measurement

The sintered pellet of $BaFe_{12}O_{19}$ was removed from the graphite mold when the surface temperature of the graphite sleeve reached room temperature. Then, the grinder was utilized to remove all graphite foil from the sintered pellet. The next step was to characterize the crystallinity of the horizontal surface of sintered specimen for estimating the texture

coefficient (TC) using X-ray diffraction (XRD, Bruker AXS D8 Advance, Karlsruhe, Ipoh, Malaysia). After that, the sintered specimen was vertically cut into two halves using the precious cutter to measure remanent magnetization for parallel ($Mr^{\parallel}$) and perpendicular ($Mr^{\perp}$) planes to the external magnetic field using vibrating sample magnetometer (VSM) (Lakshore model GMW 3474-140 Electromagnet, Westerville, Ipoh, Malaysia), as shown in Figure 3. Moreover, the applied magnetic field was 1 tesla.
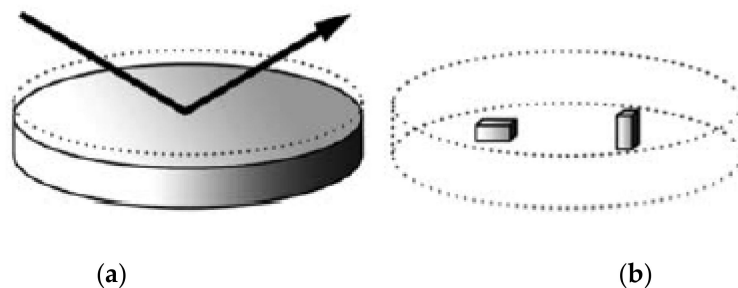

(**a**)   (**b**)

Figure 3. The scheme of (**a**) XRD of texture and (**b**) cut sample in orthogonal direction for measuring the remanent magnetization.

2.7. S/N Ratio Analysis

In this part, the optimal level for each response is calculated using Taguchi's S/N ratio analysis. For the response, such $Mr^{\parallel}$ with the-larger-the-better (LTB) quality characteristic is chosen, as in Equation (1). In contrast, for $Mr^{\perp}$, the-smaller-the-better quality characteristic is shown in Equation (2).

$$\eta_i = -10 \, log_{10} \frac{1}{N} \sum_{i=1}^{r} \left(\frac{1}{y_i{}^2} \right) \quad i = 1, \, 2, \, \dots \, r, \tag{1}$$

$$\eta_i = -10 \, log_{10} \frac{1}{N} \sum_{i=1}^{r} \left(y_i{}^2 \right) \quad i = 1, \, 2, \, \dots \, r, \tag{2}$$

where N is the number of tests, $y_i{}^2$ is the output, and η_i is the S/N ratio.

2.8. Validation

To validate the optimized parameters of the S/N ratio, the sintering of $BaFe_{12}O_{19}$ powder was conducted based on the optimized parameters. Then, all the previous steps were repeated to measure and characterize the remanent magnetization ($Mr^{\parallel}$ and $Mr^{\perp}$) and XDR, respectively. After that, Minitab 17.0 software was used to analyze linear regression and construct predictive mathematical models for the dependent variables $Mr^{\parallel}$ and $Mr^{\perp}$ as a function of holding time, cooling rate, pressure, and sintering temperature, respectively, in the current study. The collected results from predictive mathematical models were compared with the experimental results of optimized parameters.

3. Results and Discussion

3.1. Taguchi Method

A loss function is used by Taguchi, which converts the difference in experimental values and targets into an S/N ratio, which is a ratio of mean to the standard deviation. Taguchi uses signal and noise to represent the wanted and unwanted values for the response. S/N ratio has been divided into three groups: the-medium-the-better, the-larger-the-better, and the-lower-the-better based on the response requirements. In this study, the characterized quality of the responses like $Mr^{\parallel}$ and $Mr^{\perp}$ are the-larger-the-better and the-lower-the-better, respectively. Therefore, Equations (1) and (2) have been used to calculate the S/N ratio, as shown in Table 4 [44].

3.2. The Influence of Process Parameters on $(Mr^\parallel)$ and $(Mr^\perp)$

The effect of sintering parameters on $Mr^\parallel$ and $Mr^\perp$ of sintered M-type barium hexaferrite nanopowder is presented in Figure 4a–d. Where the larger the mean difference between the $Mr^\parallel$ and $Mr^\perp$, the better is the anisotropic behavior of the sintered powder. It is observed from Figure 4a that the mean difference between $Mr^\parallel$ and $Mr^\perp$ is decreased when holding time is increased. This dramatical dropping in the mean difference from 12.10 to 9.90 when the holding time increased from 60 to 180 s is caused by the dropping in the magnetic properties of the materials, where the increase in holding time leads to the decrease in the grain size which causes a reduction in the remanence magnetization of the sintered materials [35,38].
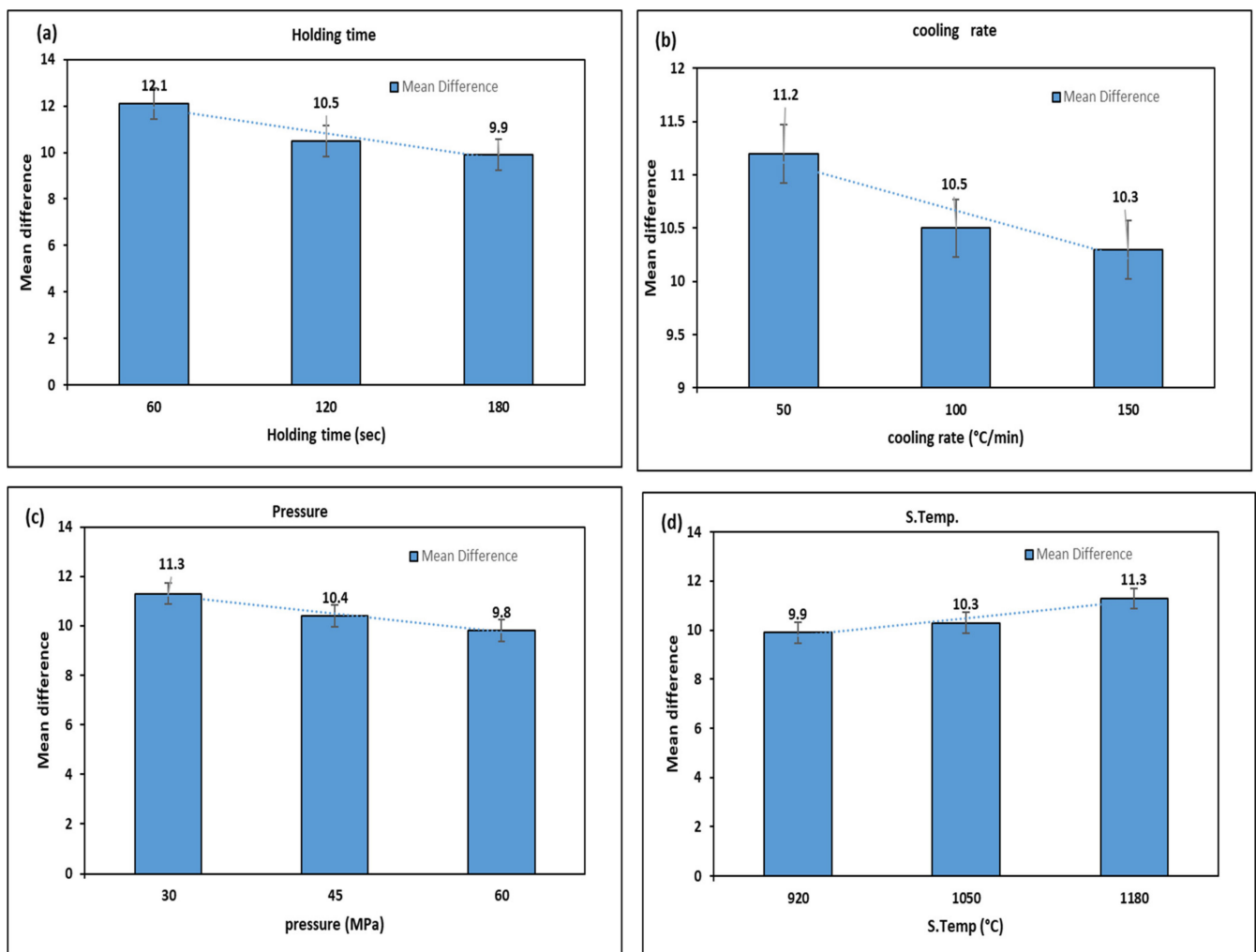

Figure 4. The effect of sintering parameters on mean difference between $Mr^\parallel$ and $Mr^\perp$: (**a**) Holding time; (**b**) Cooling rate; (**c**) Pressure; (**d**) S. temp.

The cooling rate has an impact on the mean difference between $Mr^\parallel$ and $Mr^\perp$, where the lower cooling rate results in a high mean difference. Therefore, when the value of the cooling rate is 50 (°C/min) the mean difference is 11.20, which is greater than the values of cooling rate at 100 and 150 (°C/min). This can be observed from Figure 4b where the mean differences of 100 and 150 (°C/min) are 10.5 and 10.30, respectively. The reason is that the lower cooling rate gives sufficient time for the external magnetic field to align the grains and prevent the crack to be appeared in the sintered specimen. In the previous studies, it was found that better alignment occurred at a lower cooling rate [45].

The pressure greatly influences the grains' alignment, but the low pressure exerted on the powder requires little force to rotate the grain. As the pressure increases, the external magnetic field required to align the grains increases. Furthermore, the high pressure leads to align the hexagonal crystals in the perpendicular direction to the pressure (magnetic field) [46]. As shown in Figure 4c, the mean difference is decreased from 11.30 to 10.50 when the pressure is increased from 30 to 45 MPa, respectively. It can be also observed that the mean difference is decreased to 9.80 as the pressure is further increased to 60 MPa.

As commonly known, the temperature is generated due to the increase in the electrical current that affects the reorientation of grains in the same direction of magnetic flux. Moreover, the external magnetic field and the electrical current are in proportion. In other words, the increase in electrical current leads to a rise in the temperature and external magnetic flux together. Those two factors play an important role to reorient the grains. It is important to note that the increase in temperature will increase the activation energy of particles that will assist the reorientation of grains due to the external magnetic flux [47]. In contrast to the effect of the sintering parameters mentioned above, the sintering temperature shown in Figure 4d is directly proportional to the mean difference between $Mr^{\parallel}$ and $Mr^{\perp}$ in the sense that when the temperature was 920 °C, the mean difference was 9.90. Furthermore, the increment in sintering temperature from 1050 to 1180 °C caused an increase in the mean difference of 10.30 to 11.30, respectively. This effect explained that the increment in the external magnetic field, which resulted from the high current used in rising the sintering temperature, caused a proper alignment in the grains to the easy-axis of crystalline. Furthermore, the sintering temperature caused grain growth in the c-axis which played a secondary role in increasing the remanent magnetization of the sintered sample [48].

3.3. The Optimum Selected Parameters for $Mr^{\parallel}$ and $Mr^{\perp}$

The response table for the gained S/N ratio of $Mr^{\parallel}$ is displayed in Table 5. The mean S/N ratio graph obtained using the Minitab software tool is shown in Figure 5. The minimal variance difference between the expected output and the measured output is represented by a higher S/N ratio. From Figure 5, it may be observed that the highest mean S/N ratio obtained for $Mr^{\parallel}$ occurred at 60 s holding time, 50 °C/min cooling rate, 30 MPa pressure, and 1180 °C sintering temperature. H.T. = 60 s, C.R. = 50 °C/min, P = 30 MPa, and ST 1180 °C were the predicted optimum process parameters for obtaining high remanent $Mr^{\parallel}$ in parallel to the magnetic field using the Taguchi method. The predicted combination of the optimum set was represented as $H.T._1$-$C.R._1$ -P_1 -$S.T._3$ for $Mr^{\parallel}$.

Table 5. Mean S/N ratio response table for $Mr^{\parallel}$.

Symbol	Process Parameters	Mean S/N Ratio				
		Level 1	**Level 2**	**Level 3**	**Max–Min**	**Rank**
H.T.	Holding time (s)	**26.54**	25.62	25.29	1.25	3
C.R.	Cooling rate (A/min)	**26.30**	25.69	25.46	0.84	4
P	Pressure (KN)	**26.63**	25.69	25.13	1.51	2
S.T.	S. temp. (°C)	25.10	25.67	**26.69**	1.59	1

Larger—better.

The means of the S/N ratio response table for $Mr^{\perp}$ are presented in Table 6. H.T. = 60 s, C.R. = 50 °C/min, P = 30 MPa, and S.T. = 1180 °C were the predictable optimum process parameters for obtaining the low $Mr^{\perp}$ as in Figure 6. For $Mr^{\perp}$, the predicted optimum combination was $H.T._1$–$C.R._1$ -P_1 -$S.T._3$.
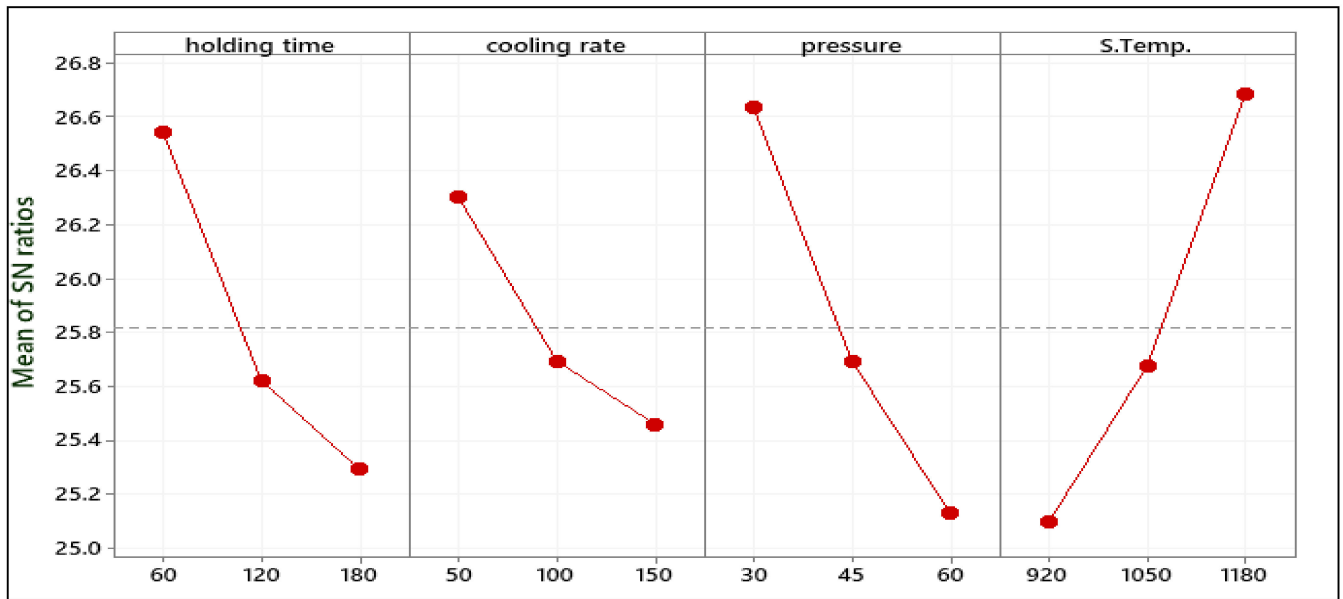
Figure 5. Mean S/N ratio of $\mathrm{Mr}^{\parallel}$.

Table 6. Mean S/N ratio response table for $\mathrm{Mr}^{\perp}$.

Symbol	Process Parameters	Mean S/N Ratio				
		Level 1	**Level 2**	**Level 3**	**Max–Min**	**Rank**
H.T.	Holding time (s)	**−20.03**	−18.89	−18.49	1.54	3
C.R.	Cooling rate (A/min)	**−19.77**	−18.99	−18.66	1.11	4
P	Pressure (KN)	**−20.17**	−18.99	−18.26	1.92	2
S.T.	S. temp. (°C)	−18.18	−18.96	**−20.27**	2.09	1

Smaller—better.

Figure 6. Mean S/N ratio of $\mathrm{Mr}^{\perp}$.
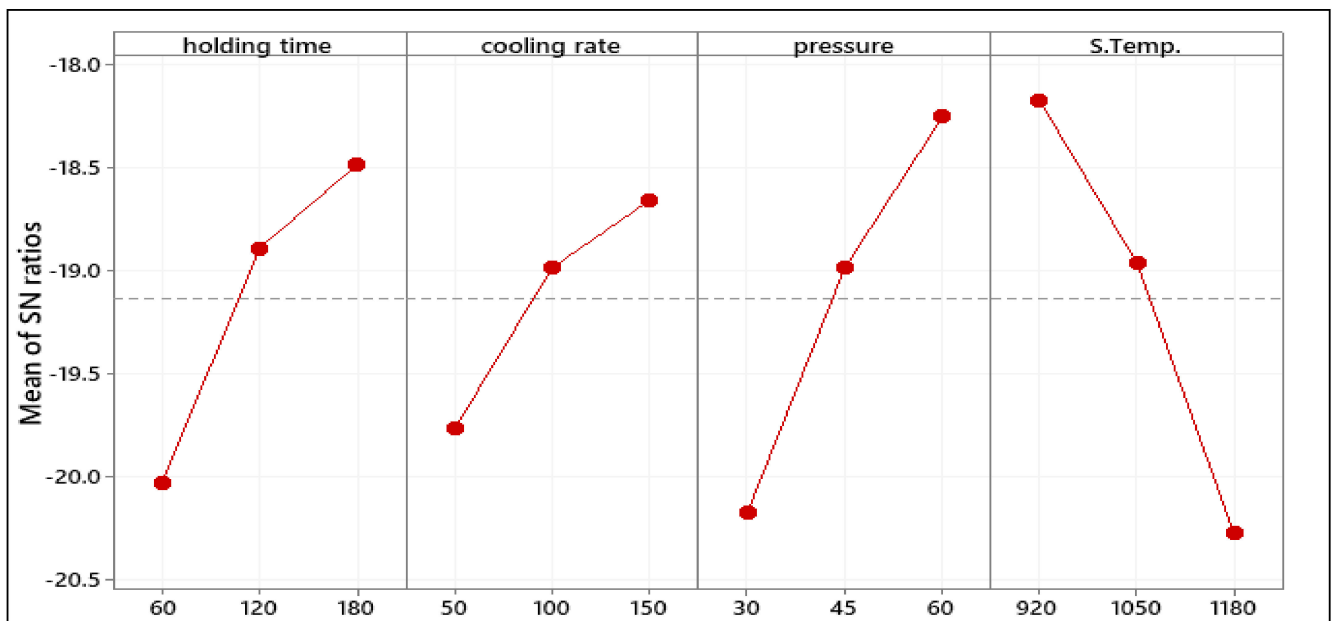
3.4. Confirmation Test

Conformational tests must be performed to validate the optimal conditions predicted by Taguchi. The response was estimated and verified using the predicted S/N ratio under predicted optimal sintering conditions. The confirmation experiments were carried out at the Taguchi predicted optimum sintering parameters, and the results are shown in Tables 7 and 8 for $Mr^\parallel$ and $Mr^\perp$, respectively. The predicted optimum sintering parameters for both $Mr^\parallel$ and $Mr^\perp$ give an enhancement in the performance representative results. Tables 7 and 8 show that for both $Mr^\parallel$ and $Mr^\perp$, the S/N ratios of predicted and optimal sintering processes are very close. The improved S/N ratios for $Mr^\parallel$ and $Mr^\perp$ were found at the optimum sintering parameters with 5.23 dB and 6.09 dB values, respectively, compared to the initial settings. Tables 7 and 8 display the confirmation results of $Mr^\parallel$ and $Mr^\perp$. The optimum predicted parameters given by Taguchi provide better results than the initial parameter conditions according to the confirmation experiments. Hence, the increment in $Mr^\parallel$ and the reduction in $Mr^\perp$ were 26.56% and 27.83%, respectively.

Table 7. Confirmation test results for $Mr^\parallel$.

	Optimal Process Parameters		
	Initial Process Parameters	**Prediction**	**Experimental**
Levels	$(H.T.)_2$-$(C.R.)_2$-P_2-$(S.T.)_2$	$(H.T.)_1$-$(C.R.)_1$-P_1-$(S.T.)_3$	$(H.T.)_1$-$(C.R.)_1$-P_1-$(S.T.)_3$
$Mr^\parallel$	19.91	28.71	27.11
S/N ratio (dB)	24.84		29.72
Improvement in S/N ratio (dB)	5.23		
Percentage of the increment in $Mr^\parallel$ (emu/g)	26.56%		

Table 8. Confirmation test results for $Mr^\perp$.

	Optimal Process Parameters		
	Initial Process Parameters	**Prediction**	**Experimental**
Levels	$(H.T.)_2$-$(C.R.)_2$-P_2-$(S.T.)_2$	$(H.T.)_1$-$(C.R.)_1$-P_1-$(S.T.)_3$	$(H.T.)_1$-$(C.R.)_1$-P_1-$(S.T.)_3$
$Mr^{222.}$	9.87	-22.83	7.72
S/N ratio (dB)	-19.91		-26.01
Improvement in S/N ratio (dB)	6.09		
Percentage of the reduction in $Mr^\perp$ (emu/g)	27.83%		

3.5. XRD Analysis

The grain orientation and phase analyses were conducted using an XRD system. The relative intensity ratio between (006) and (114) peaks (I_{006}/I_{114}) was determined for the samples sintered at the initial sintering parameters and at the optimized sintering parameters taken from Taguchi result as shown in Figure 7a–c, where the increase in the relative intensity means that the grains lead to be reoriented along the c-axis (highly textured) [49]. Accordingly, the orientation of the grain can be obtained qualitatively by the Texture Coefficient (TC) [50]. TC value can be calculated as in Equation (3) [51]:

$$TC_{(hkl)} = \frac{I_{(hkl)} / I_{0(hkl)}}{\left(\frac{1}{N}\right)\left[\sum_N \frac{I_{(hkl)}}{I_{0(hkl)}}\right]} \tag{3}$$

where, $I_{0(hkl)}$, and $I_{(hkl)}$ represent the standard and the measured relative intensities of the specific crystal plans (hkl), and N represents the number of peaks. The calculated TC values are displayed in Table 9.
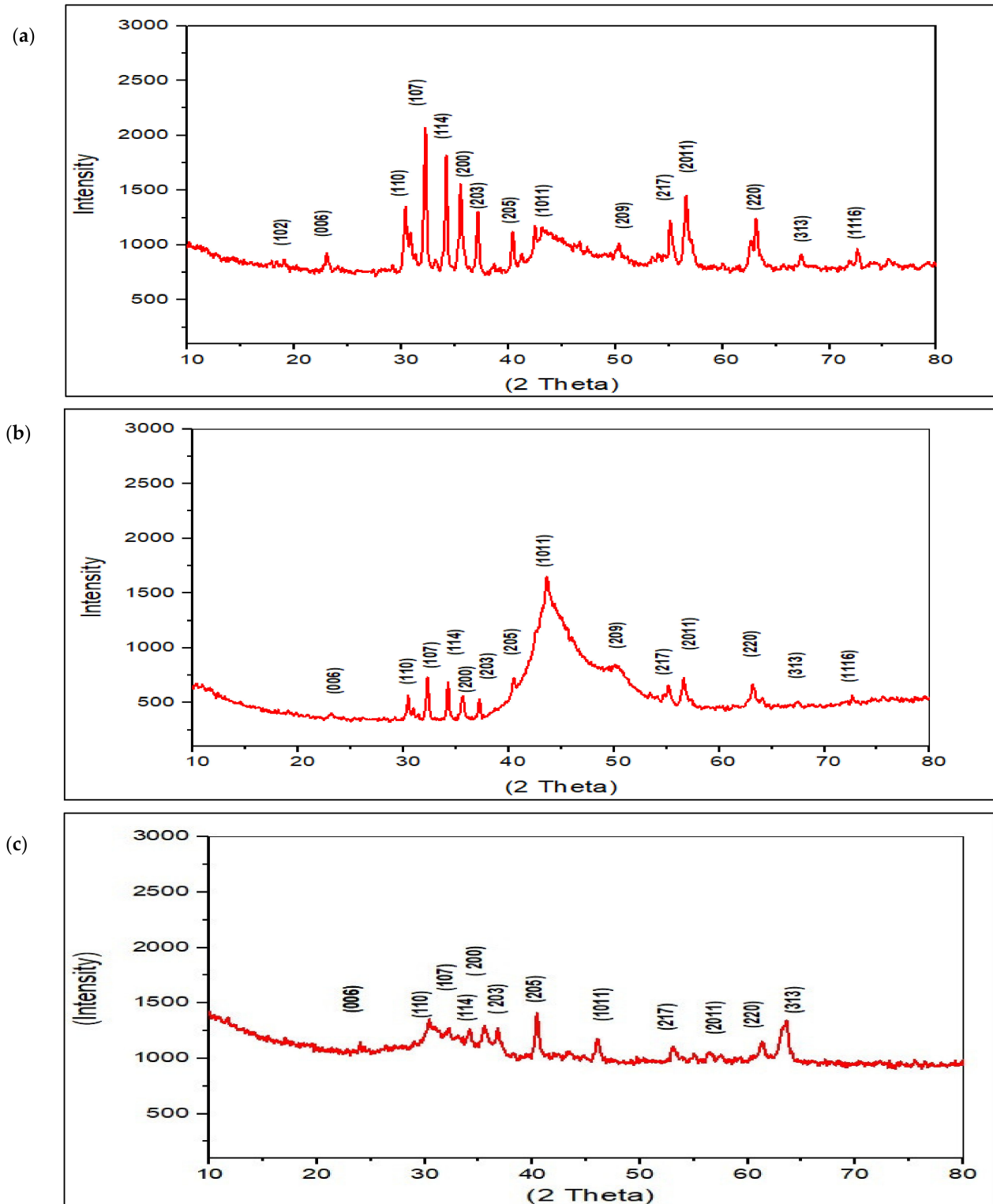

Figure 7. XRD of (**a**) Sintered sample at the optimized parameters; (**b**) Sintered sample at the initial parameters, and (**c**) Starting powder used in this study.

Table 9. Texture coefficient (TC).

Sample	Crystal Plane					
	(006)	**(107)**	**(114)**	**(1011)**	**(217)**	**(313)**
Intial process parameters	11.90	3.50	2.00	6.40	2.00	1.20
Optimized parameters	12.20	4.40	1.70	5.90	1.50	0.80

The relative intensity ratio (I_{006}/I_{114}) of the sintered sample at the initial process parameters is 40.60, and this value was improved for the sample with the optimized parameters to 51.23. This increase in the relative intensity demonstrated that the grains are oriented along the c-axis. The broadening occurs, as seen in Figure 7c, in between 40 and 50 of 2θ indicates the grain refinement and high lattice strain [52]. The amorphization which can be observed from the decrease in the intensities of the peak has resulted from the graphite foil used during the sintering, where the increase in the intensity of the peak (1011) matched the highest peak intensity of the graphite.

These findings were also proved by the TC. Table 9 clearly shows that the (006) plane of the two samples have the highest TC values, indicating that all of the samples have a c-axis desired orientation. It is important to note that the TC value of plane (006) of the sample sintered at the optimized parameters is higher than that of the initial parameters. In contrast, the TC value of the plane (114) decreased from 2.0 to 1.70 of the samples sintered at the initial and optimized parameters, respectively. Thus, this confirms that the preferred growth orientation of $BaFe_{12}O_{19}$ is along the c-axis.

4. ANOVA Analysis

ANOVA identifies the process variable that has the greatest influence on the output. Tables 10 and 11 show the ANOVA results for $Mr^{\parallel}$ and $Mr^{\perp}$, respectively. According to Table 10, sintering temperature has the greatest influence on $Mr^{\parallel}$, followed by pressure, holding time, and cooling rate. Sintering temperature, pressure, holding time, and cooling rate contributed to $Mr^{\parallel}$ by 35.25%, 31.48%, 22.95%, and 10.32%, correspondingly, as indicated in Table 10. Similarly, $Mr^{\perp}$ was typically influenced by sintering temperature, pressure, holding time, and cooling rate. The respective percentages contribution of sintering temperature followed by pressure, holding time, and cooling rate were 36.99%, 31.02%, 21.24%, and 10.74%, respectively, as shown in Table 11. Due to the magnetic field being influenced by the current used for heat generation, the ANOVA study revealed that both $Mr^{\parallel}$ and $Mr^{\perp}$ were significantly affected by the sintering temperature.

Table 10. ANOVA for $Mr^{\parallel}$.

Source	Degree of Freedom	Sum of Square	Means Square	% Contributions
H.T. (s)	2	2.53	1.26	22.95
C.R. (A/min)	2	1.13	0.56	10.32
P (MPa)	2	3.47	1.73	31.48
S.T. (°C)	2	3.89	1.94	35.25
Total	8	11.03		100

Table 11. ANOVA FOR $Mr^{\perp}$.

Source	Degree of Freedom	Sum of Square	Means Square	% Contributions
H.T. (s)	2	3.84	1.92	21.24
C.R. (A/min)	2	1.94	0.97	10.74
P (MPa)	2	5.62	2.80	31.02
S.T. (oC)	2	6.70	3.35	36.99
Total	8	18.11		100

5. Modeling

The Equations (4) and (5) were driven from the linear regression to predict the values for $Mr^{\parallel}$ and $Mr^{\perp}$, respectively.

$$Mr^{\mid} = 15.75 - 0.02261 \text{ H.T.} - 0.01920 \text{ C.R.} - 0.669 \text{ P} + 0.01295 \text{ S.T.} \tag{4}$$

(R2 = 95.59%)

$$Mr = 6.62 - 0.01269 \text{ H.T.} - 0.01170 \text{ C.R.} - 0.3940 \text{ P} + 0.00781 \text{ S.T.} \tag{5}$$

(R2 = 95.74%)

The developed regression models of $Mr^{\parallel}$ and $Mr^{\perp}$ have a high coefficient of determination R^2 values of 95.59% and 95.74%. This indicates that the dependent and independent variables in the established model are well-matched. The significance of the coefficient in the forecast model was validated by the residual plot. In contrast, the model's error is considered normally distributed and significant when the plot is in a straight line. As observed from Figures 8 and 9, the residual of the $Mr^{\parallel}$ and $Mr^{\perp}$ are near a straight line, implying that the developed models are significant.
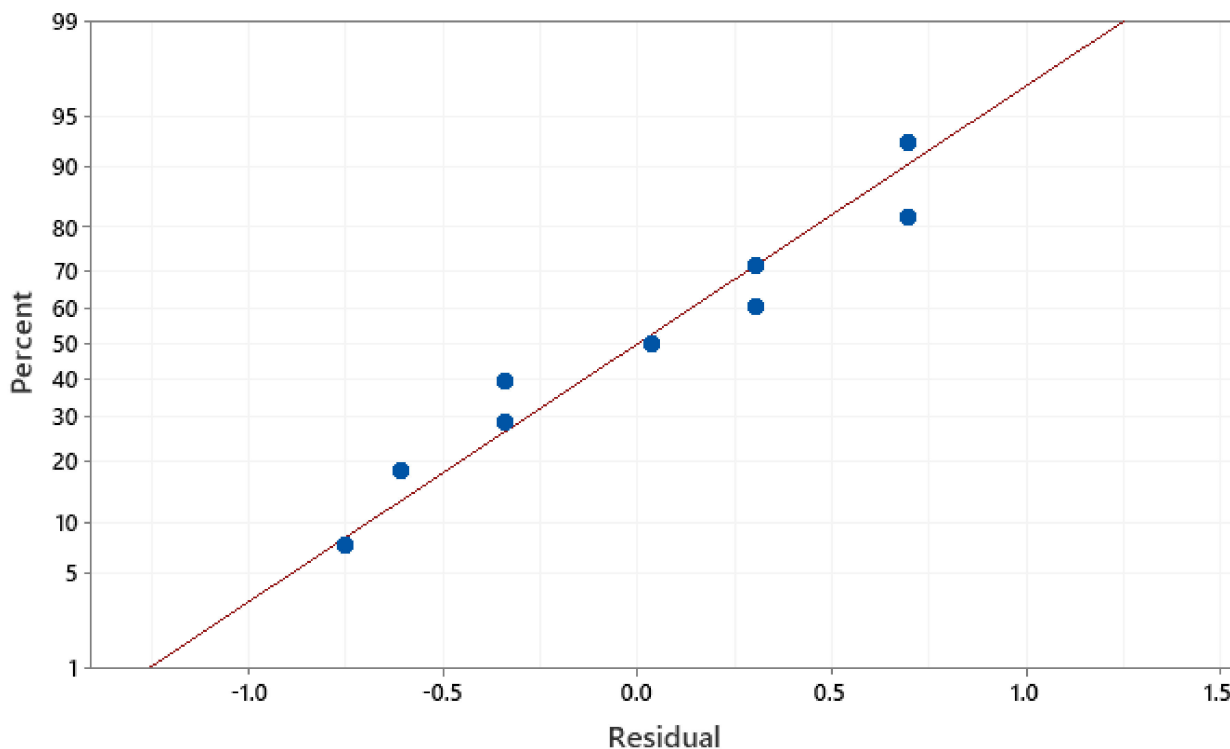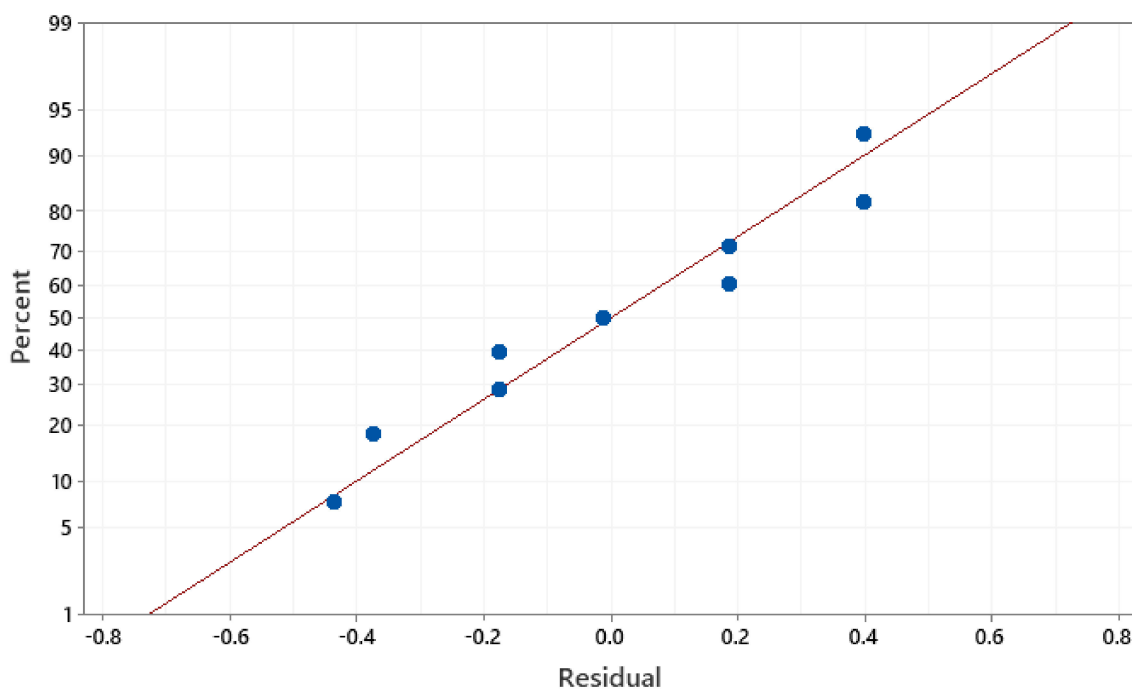

Figure 8. Normal probability plot of the residuals for $Mr^{\parallel}$.

Confirmation tests were used to validate the built models, and the tested results were selected randomly from the configuration of the experimental matrix. The results verified that the predicted and experimental values were in good agreement with the parameters described in Table 12.

Table 12. The confirmed results for the developed model.

	Experimental		Predicted		Residuals		% Error	
Run	$Mr^{\parallel}$ (emu/g)	$Mr^{\perp}$ (emu/g)	$Mr^{\parallel}$ (emu/g)	$Mr^{\perp}$ (emu/g)	$Mr^{\parallel}$ (emu/g)	$Mr^{\perp}$ (emu/g)	$Mr^{\parallel}$ (emu/g)	$Mr^{\perp}$ (emu/g)
2	20.30	9.50	19.69	9.17	−0.60	−0.32	2.97	3.44
5	16	7	16.35	7.18	0.355	0.18	2.21	2.57
8	22	10.6	23.05	11.17	1.05	0.57	4.78	5.40
9	16	7	15.70	6.81	−0.29	−0.18	1.81	2.58

Figure 9. Normal probability plot of the residuals for $Mr^{\perp}$.

Contour plots can analyze the relationship between the response and two variables by viewing distinct contours of the expected response variables. The contour plots shown in Figure 10 represent the relation between the sintering parameters and the remanent magnetization in the parallel axis with external magnetic field $Mr^{\parallel}$ values. Figure 10a shows that the low level of holding time and cooling rate generates a high $Mr^{\parallel}$ value. Figure 10b indicates that high $Mr^{\parallel}$ could be attained when the pressure ranged between 40 and 45 MPa and holding time between 100 and 120 s. It was observed in Figure 10c that $Mr^{\parallel}$ is maximum when the cooling rate and pressure ranged between 50 and 100 °C/min and 30–35 MPa, respectively. High sintering temperature with high holding time leads to high $Mr^{\parallel}$ as in Figure 10d. With high sintering temperature and cooling rate in between 75 and 100 s, the $Mr^{\parallel}$ increases, as in Figure 10e.

Similarly, in Figure 10f, the high value of $Mr^{\parallel}$ was obtained at high sintering temperature and pressure ranged between 35 and 40 MPa. The relation between the $Mr^{\perp}$ and the variables is presented in Figure 11. From the observed data, the sintering temperature contributed to the increase of the remanent magnetization of the whole sample from different directions. The remanent magnetization in the perpendicular direction increased with the increase in samples' overall remanent of about 50% of the $Mr^{\parallel}$. The other parameters have the same effect on the $Mr^{\perp}$ and $Mr^{\parallel}$.
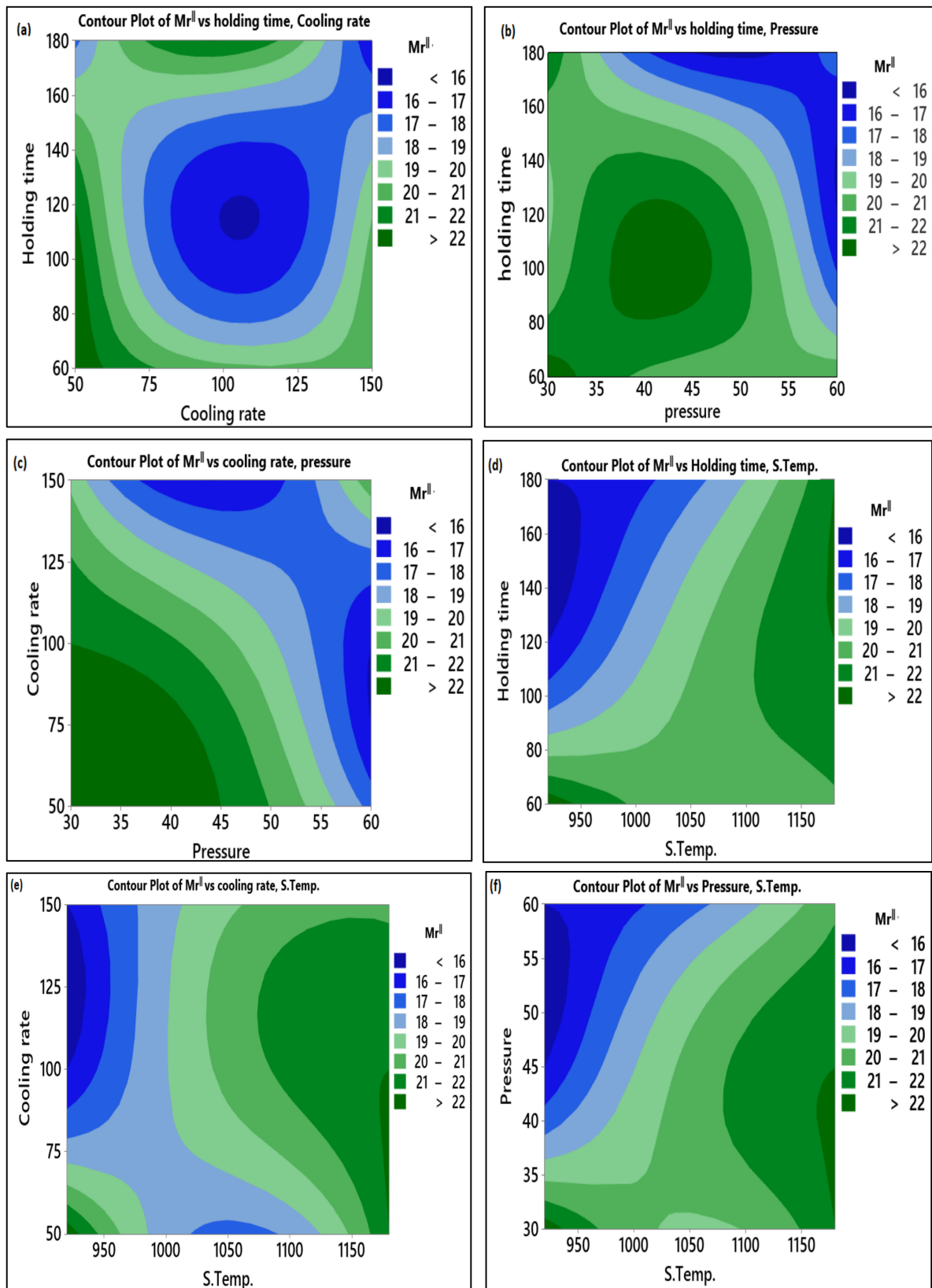
Figure 10. Contour plot for Mr$^{\parallel}$: (**a**) Holding time vs. cooling rate; (**b**) Holding time vs. pressure; (**c**) Cooling rate vs. pressure; (**d**) Holding time vs. S. temp.; (**e**) Cooling rate vs. S. temp.; (**f**) Pressure vs. S. temp.
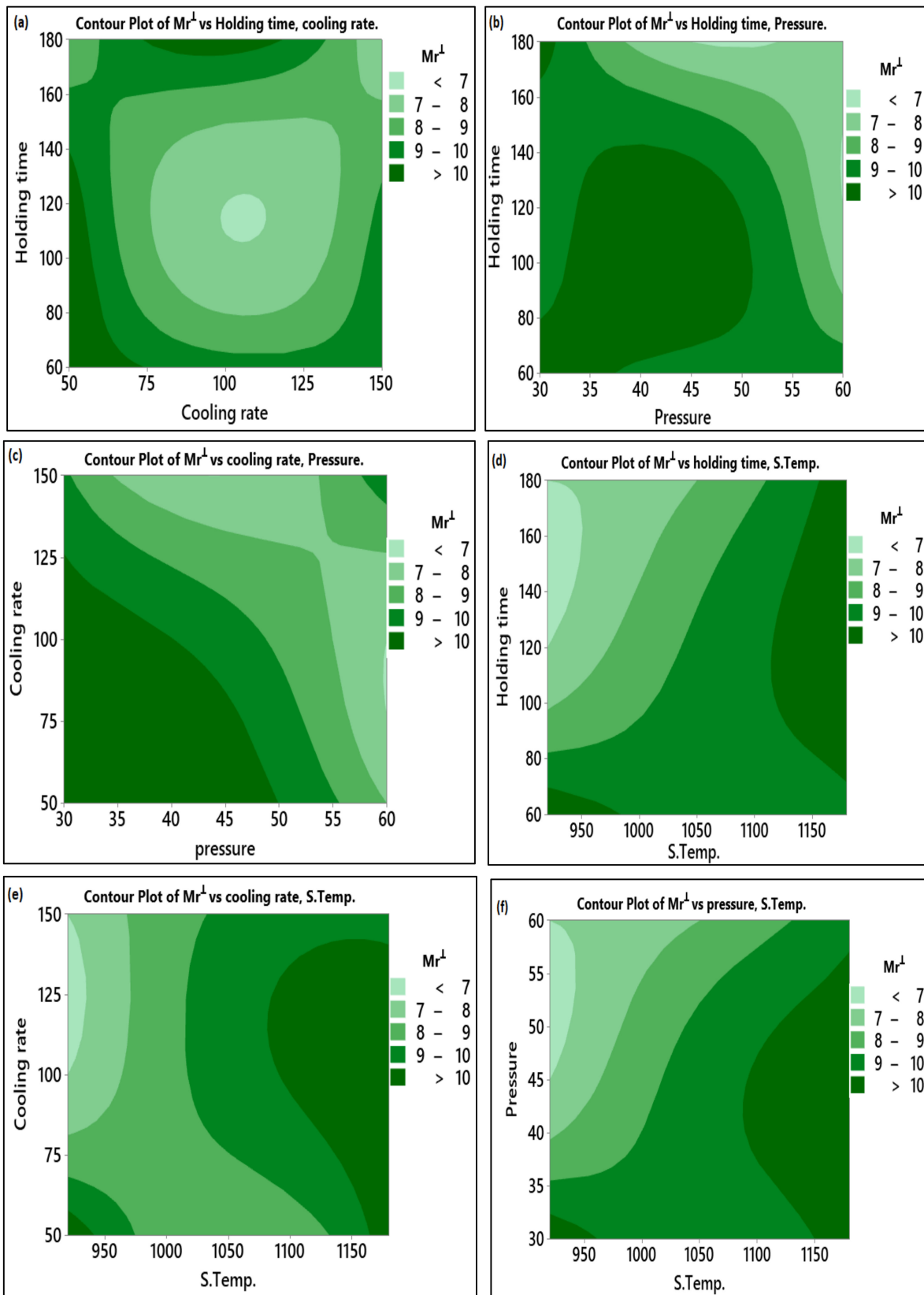
Figure 11. Contour plot for $Mr^{\perp}$: (**a**) Holding time vs. cooling rate; (**b**) Holding time vs. pressure; (**c**) Cooling rate vs. pressure; (**d**) Holding time vs. S. temp.; (**e**) Cooling rate vs. S. temp.; (**f**) Pressure vs. S. temp.

6. Assessment of $Mr^{\parallel}$ and $Mr^{\perp}$ for Sintered $BaFe_{12}O_{19}$

$Mr^{\parallel}$ and $Mr^{\perp}$ of sintered $BaFe_{12}O_{19}$ by using different sintering technology and MASPS were compared and listed in Table 13. The $Mr^{\parallel}$ and $Mr^{\perp}$ values of SPS with NaCl are found to be 29.30 and 24.90, respectively. On the other hand, the $Mr^{\parallel}$ and $Mr^{\perp}$ values of MASPS are 27.10 and 7.70, respectively, which shows that SPS with NaCl resulted with higher values of $Mr^{\parallel}$ and $Mr^{\perp}$. This comparison does not evidentially represent the better anisotropic behavior of the sintered sample by SPS with NaCl, rather the anisotropic behavior is represented by the relative ratio between $Mr^{\parallel}$ and $Mr^{\perp}$. In that sense, the relative ratio of the sintered sample by MASPS is 71.61%, which is higher than that of the SPS with NaCl with a value of 26%. This analysis shows that the anisotropic behavior of MASPS is better than that of SPS with NaCl. The high $Mr^{\parallel}$ and $Mr^{\perp}$ values of SPS with NaCl can be justified by the presence of high grain-size powder.

Table 13. $Mr^{\parallel}$ and $Mr^{\perp}$ values of sintered $BaFe_{12}O_{19}$ with different methods.

Method	$Mr^{\parallel}$ (emu/g)	$Mr^{\perp}$ (emu/g)	References
Magnetic-field-assisted hydrothermal process	23.10	-	[53]
SPS with NaCl	29.30	24.90	[32]
SPS with protection layer	13.00	9.50	[17]
SPS	19.00	-	[28]
Powder injection molding	9.00	3.60	[54]
MASPS	27.10	7.70	Current study

7. Conclusions

Anisotropic $BaFe_{12}O_{19}$ magnets were achieved by a developed magnetic-anisotropy spark plasma sintering at the low magnetic field coupled with sintering current. From the analyzed results, the following conclusions were drawn:

- The optimum setting sintering parameters for obtaining the high $Mr^{\parallel}$ was found as H.T. = 60 s, C.R. = 50 °C/min, P = 30 MPa and S.T. = 1180 °C ($(H.T.)_1$-$(C.R.)_1$-P_1-$(S.T.)_3$) using Taguchi method. It was observed that a 26.57% increment of $Mr^{\parallel}$ was found at the Taguchi determined optimum sintering condition.
- The optimum sintering combination for $Mr^{\perp}$ determined by the Taguchi method is the same as the combination for obtaining $Mr^{\parallel}$. In contrast, the increment in the remanence of the sintered sample in the parallel direction leads to a decrease in the remanence of the perpendicular direction in about 50% of $Mr^{\parallel}$. In the Taguchi optimized sintering condition, the amount of reduction in the $Mr^{\perp}$ was 27.83%.
- It was observed from the ANOVA analysis that $Mr^{\parallel}$ and $Mr^{\perp}$ were significantly influenced by the sintering temperature with a contribution of 35.25% and 36.99%, respectively, followed by pressure, holding time, and cooling rate.
- Based on the well-founded optimal sintering parameters, it can be suggested that MASPS with a high magnetic field could be a promising approach to achieve anisotropic permanent magnets because both $Mr^{\parallel}$ and $Mr^{\perp}$ can be tailored to reach the desired properties.
- From the XRD, the improvement in the relative intensity ratio between (006) and (114) peaks (I_{006}/I_{114}) from 40.60 to 51.29 for the sintered powder at the initial and optimized process parameters proved that the grains have been oriented along the c-axis, which was also supported by the TC values of the plane.
- From the developed mathematical models $Mr^{\parallel}$ and $Mr^{\perp}$, a close agreement between the predicted results and experimental results was observed. Hence, the developed models could correct sintering parameters for producing anisotropic magnets without conducting trial experiments.
- Further studies are recommended to investigate the effect of process parameters of MASPS on the mechanical and microstructure behavior of the sintered nanopowder.

References

1. Benito, G.; Morales, M.; Requena, J.; Raposo, V.; Vázquez, M.; Moya, J. Barium hexaferrite monodispersed nanoparticles prepared by the ceramic method. *J. Magn. Magn. Mater.* **2001**, *234*, 65–72. [CrossRef]
2. El Shater, R.; El-Ghazzawy, E.; El-Nimr, M. Study of the sintering temperature and the sintering time period effects on the structural and magnetic properties of M-type hexaferrite $BaFe_{12}O_{19}$. *J. Alloy. Compd.* **2018**, *739*, 327–334. [CrossRef]
3. Ahmad, M.; Ali, Q.; Ali, I.; Ahmad, I.; Khan, M.A.; Akhtar, M.N.; Murtaza, G.; Rana, M. Effects of Sr-substitution on the structural and magnetic behavior of Ba-based Y-type hexagonal ferrites. *J. Alloy. Compd.* **2013**, *580*, 23–28. [CrossRef]
4. Chao, Y.; Lin, J.; Chun, S.; Kim, K. Temperature dependent spin structures in Hexaferrite crystal. *J. Magn. Magn. Mater.* **2016**, *397*, 230–232. [CrossRef]
5. Shepherd, P.; Mallick, K.K.; Green, R.J. Magnetic and structural properties of M-type barium hexaferrite prepared by co-precipitation. *J. Magn. Magn. Mater.* **2007**, *311*, 683–692. [CrossRef]
6. Thompson, G.K.; Evans, B.J. The structure–property relationships in M-type hexaferrites: Hyperfine interactions and bulk magnetic properties. *J. Appl. Phys.* **1993**, *73*, 6295–6297. [CrossRef]
7. Rowley, S.E.; Chai, Y.-S.; Shen, S.-P.; Sun, Y.; Jones, A.T.; Watts, B.E.; Scott, J.F. Uniaxial ferroelectric quantum criticality in multiferroic hexaferrites $BaFe_{12}O_{19}$ and $SrFe_{12}O_{19}$. *Sci. Rep.* **2016**, *6*, 25724. [CrossRef] [PubMed]
8. Thakur, A.; Singh, R.; Barman, P. Synthesis and characterizations of Nd3+ doped $SrFe_{12}O_{19}$ nanoparticles. *Mater. Chem. Phys.* **2013**, *141*, 562–569. [CrossRef]
9. Kaynar, M.B.; Ozcan, S.; Shah, S.I. Synthesis and magnetic properties of nanocrystalline $BaFe_{12}O_{19}$. *Ceram. Int.* **2015**, *41*, 11257–11263. [CrossRef]
10. Idayanti, N.; Kristiantoro, T.; Septiani, A.; Kartika, I. Magnetic properties of barium ferrite after milling by high energy milling (hem). *MATEC Web Conf.* **2017**, *101*, 1011. [CrossRef]
11. Kumar, P.; Anurag, G. Signature of multiferroicity and pyroelectricity close to room temperature in $BaFe_{12}O_{19}$ hexaferrite. *Ceram. Int.* **2017**, *43*, 16403–16407. [CrossRef]
12. Pan, X.F.; Mu, G.H.; Chen, N.; Gan, K.K.; Yang, K.; Gu, M.Y. Improved properties of $SrFe_{12}O_{19}$ synthesised by gel self-propagating combustion technique with glycol as solvent. *Mater. Sci. Technol.* **2007**, *23*, 865–868. [CrossRef]
13. Drofenik, M.; Ban, I.; Makovec, D.; Žnidaršič, A.; Jagličić, Z.; Hanžel, D.; Lisjak, D. The hydrothermal synthesis of super-paramagnetic barium hexaferrite particles. *Mater. Chem. Phys.* **2011**, *127*, 415–419. [CrossRef]
14. Sözeri, H. Effect of pelletization on magnetic properties of $BaFe_{12}O_{19}$. *J. Alloy. Compd.* **2009**, *486*, 809–814. [CrossRef]
15. Meng, S.; Yue, Z.; Li, L. In-plane c-axis oriented barium hexaferrite films prepared by magnetron sputtering. *Mater. Lett.* **2012**, *86*, 92–95. [CrossRef]
16. Kang, S.-J.L.; Park, J.-H.; Ko, S.-Y.; Lee, H.-Y. Solid-State Conversion of Single Crystals: The Principle and the State-of-the-Art. *J. Am. Ceram. Soc.* **2015**, *98*, 347–360. [CrossRef]
17. Lisjak, D.; Ovtar, S. The Alignment of Barium Ferrite Nanoparticles from Their Suspensions in Electric and Magnetic Fields. *J. Phys. Chem. B* **2012**, *117*, 1644–1650. [CrossRef] [PubMed]
18. Yamada, H.; Suzuki, T.S.; Uchikoshi, T.; Hozumi, M.; Saito, T.; Sakka, Y. Ideal design of textured $LiCoO_2$ sintered electrode for Li-ion secondary battery. *APL Mater.* **2013**, *1*, 042110. [CrossRef]
19. Zeng, J.; Li, Y.; Yang, Q.; Jing, X.; Yin, Q. Grain oriented $CaBi_4Ti_4O_{15}$ piezoceramicsprepared by the screen-printing multilayer grain growth technique. *J. Eur. Ceram. Soc.* **2005**, *25*, 2727–2730. [CrossRef]

20. Imai, A.; Nagarajan, V.; Takahashi, R.; Lippmaa, M.; Matsumoto, Y. Self-template growth of ferroelectric Bi4Ti3O12nanoplates via flux-mediated epitaxy withVOx. *Cryst. Growth Des.* **2010**, *10*, 5233–5237. [CrossRef]
21. Zhigadlom, N.D. Growth of whisker-like and bulk single crystals of PrFeAs(O, F) under high pressure. *J. Cryst. Growth.* **2013**, *382*, 75–79. [CrossRef]
22. Sovizi, S.; Seraji, M. The densification behavior of metals and alloys during spark plasma sintering: A mini-review. *Sci. Sinter.* **2019**, *51*, 135–152. [CrossRef]
23. Nečina, V.; Pabst, W. Influence of the heating rate on grain size of alumina ceramics prepared via spark plasma sintering (SPS). *J. Eur. Ceram. Soc.* **2020**, *40*, 3656–3662. [CrossRef]
24. Garay, J. Current-Activated, Pressure-Assisted Densification of Materials. *Annu. Rev. Mater. Res.* **2010**, *40*, 445–468. [CrossRef]
25. Orrù, R.; Licheri, R.; Locci, A.M.; Cincotti, A.; Cao, G. Consolidation/synthesis of materials by electric current activated/assisted sintering. *Mater. Sci. Eng. R Rep.* **2009**, *63*, 127–287. [CrossRef]
26. Albaaji, A.J.; Castle, E.G.; Reece, M.J.; Hall, J.P.; Evans, S.L. Influence of spark plasma sintering parameters on magnetic properties of FeCo alloy. *AIP Adv.* **2018**, *8*, 047705. [CrossRef]
27. Mohammed, H.G.; Albarody, T.M.B.; Mustapha, M.; Sultan, N.; Al-Jothery, H. Investigate the effect of process parameters of magnetic inductively assisted spark plasma sintering (SPS) of iron oxide (Fe_3O_4) on microstructure behavior—Part I. *Mater. Today Proc.* **2021**, *42*, 2106–2112. [CrossRef]
28. Jung, I.D.; Kim, Y.; Hong, Y.-K.; Park, S.J. Spark Plasma Sintering Behaviors of M-type Barium Hexaferrite Nano Powders. *J. Korean Powder Met. Inst.* **2014**, *21*, 256–259. [CrossRef]
29. Zhao, W.; Wei, P.; Wu, X.; Wang, W.; Zhang, Q. Evidence and role of excessive iron in the lattice of M-type barium hexaferrite synthesized by one-step spark plasma sintering method. *Scr. Mater.* **2008**, *59*, 282–285. [CrossRef]
30. Mazaleyrat, F.; Pasko, A.; Bartok, A.; LoBue, M. Giant coercivity of dense nanostructured spark plasma sintered barium hexaferrite. *J. Appl. Phys.* **2011**, *109*, 7. [CrossRef]
31. Ovtar, S.; Le Gallet, S.; Minier, L.; Millot, N.; Lisjak, D. Control of barium ferrite decomposition during spark plasma sintering: Towards nanostructured samples with anisotropic magnetic properties. *J. Eur. Ceram. Soc.* **2014**, *34*, 337–346. [CrossRef]
32. An, G.-H.; Hwang, T.-Y.; Kim, J.; Kim, J.; Kang, N.; Jeon, K.-W.; Kang, M.; Choa, Y.-H. Novel method for low temperature sintering of barium hexaferrite with magnetic easy-axis alignment. *J. Eur. Ceram. Soc.* **2014**, *34*, 1227–1233. [CrossRef]
33. Saito, T. Magnetic properties of Sm–Fe–N anisotropic magnets produced by magnetic-field-assisted spark plasma sintering. *Mater. Sci. Eng. B* **2010**, *167*, 75–79. [CrossRef]
34. Ouar, N.; Schoenstein, F.; Mercone, S.; Farhat, S.; Villeroy, B.; Leridon, B.; Jouini, N. Spark-plasma-sintering magnetic field assisted compaction of Co80Ni20 nanowires for anisotropic ferromagnetic bulk materials. *J. Appl. Phys.* **2013**, *114*, 163907. [CrossRef]
35. Chen, Y.-C.; Gregori, G.; Rheingans, B.; Huang, W.; Kronmüller, H.; Schütz, G.; Goering, E. Magnetic and microstructural properties of anisotropic MnBi magnets compacted by spark plasma sintering. *J. Alloy. Compd.* **2020**, *830*, 154605. [CrossRef]
36. Neamţu, B.; Chicinaş, I.; Isnard, O.; Ciascai, I.; Chiriac, H.; Lostun, M. Magnetic properties of nanocrystalline Ni3Fe compacts prepared by spark plasma sintering. *Intermetallics* **2013**, *35*, 98–103. [CrossRef]
37. Munir, Z.A.; Anselmi-Tamburini, U.; Ohyanagi, M. The effect of electric field and pressure on the synthesis and consolidation of materials: A review of the spark plasma sintering method. *J. Mater. Sci.* **2006**, *41*, 763–777. [CrossRef]
38. Singh, L.K.; Bhadauria, A.; Jana, S.; Laha, T. Effect of Sintering Temperature and Heating Rate on Crystallite Size, Densification Behaviour and Mechanical Properties of Al-MWCNT Nanocomposite Consolidated via Spark Plasma Sintering. *Acta Met. Sin. Engl. Lett.* **2018**, *31*, 1019–1030. [CrossRef]
39. Mortazavi, B.; Pereira, L.F.C.; Jiang, J.-W.; Rabczuk, T. Modelling heat conduction in polycrystalline hexagonal boron-nitride films. *Sci. Rep.* **2015**, *5*, 13228. [CrossRef]
40. Mortazavi, B.; Rabczuk, T. Multiscale modeling of heat conduction in graphene laminates. *Carbon* **2015**, *85*, 1–7. [CrossRef]
41. Ogunbiyi, O.; Jamiru, T.; Sadiku, R.; Adesina, O.; Olajide, J.L.; Beneke, L. Optimization of spark plasma sintering parameters of inconel 738LC alloy using response surface methodology (RSM). *Int. J. Light. Mater. Manuf.* **2020**, *3*, 177–188. [CrossRef]
42. Khajelakzay, M.; Bakhshi, S.R. Optimization of spark plasma sintering parameters of Si 3 N 4 -SiC composite using response surface methodology (RSM). *Ceram. Int.* **2017**, *43*, 6815–6821. [CrossRef]
43. Ujah, C.O.; Popoola, A.P.I.; Popoola, O.M.; Aigbodion, V.S. Optimisation of spark plasma sintering parameters of Al-CNTs-Nb nano-composite using Taguchi Design of Experiment. *Int. J. Adv. Manuf. Technol.* **2018**, *100*, 1563–1573. [CrossRef]
44. Taguchi, G. *Engineering Methods to Optimise Quality and Minimise Costs*; Quality Resources: Milwaukee, WI, USA, 1987; pp. 1–85.
45. Radhakrishnan, B.; Nicholson, D.; Eisenbach, M.; Parish, C.; Ludtka, G.; Rios, O. Alignment of iron nanoparticles in a magnetic field due to shape anisotropy. *J. Magn. Magn. Mater.* **2015**, *394*, 481–490. [CrossRef]
46. Korent, M.; Komelj, M.; Šturm, S.; Rožman, K.Ž.; Kobe, S.; Soderžnik, K.Ž.; Soderžnik, M. Magnetic properties and microstructure evolution of hot-deformed Nd-Fe-B magnets produced by low-pressure spark-plasma sintering. *J. Magn. Magn. Mater.* **2020**, *515*, 167279. [CrossRef]
47. Bolarín-Miró, A.; Jesús, F.S.-D.; Cortés-Escobedo, C.; La Torre, S.D.-D.; Valenzuela, R. Synthesis of M-type $SrFe_{12}O_{19}$ by mechanosynthesis assisted by spark plasma sintering. *J. Alloy. Compd.* **2015**, *643*, S226–S230. [CrossRef]
48. Sardjono, P.; Gulo, F.; Setiabudidaya, D. Effect of Sintering Temperature to Physical, Magnetic Properties and Crystal Structure on Permanent Magnet $BaFe_{12}O_{19}$ Prepared from Mill Scale. *IOP Conf. Series: Mater. Sci. Eng.* **2017**, *214*, 12009.

49. An, S.; Zhang, T.; Jiang, C. Magnetic texture and coercivity of anisotropic nanocrystalline SmCo6.1Si0.9 magnets. *J. Appl. Phys.* **2014**, *115*, 17. [CrossRef]

50. Putri, N.A.; Fauzia, V.; Iwan, S.; Roza, L.; Umar, A.A.; Budi, S. Mn-doping-induced photocatalytic activity enhancement of ZnO nanorods prepared on glass substrates. *Appl. Surf. Sci.* **2018**, *439*, 285–297. [CrossRef]

51. Sönmezoğlu, S.; Akman, E. Improvement of physical properties of ZnO thin films by tellurium doping. *Appl. Surf. Sci.* **2014**, *318*, 319–323. [CrossRef]

52. Nagarjuna, C.; Dharmaiah, P.; Kim, K.B.; Hong, S.-J. Grain refinement to improve thermoelectric and mechanical performance in n-type Bi2Te2.7Se0.3 alloys. *Mater. Chem. Phys.* **2020**, *256*, 123699. [CrossRef]

53. Zhang, M.; Dai, J.; Liu, Q.; Li, Q.; Zi, Z. Fabrication and magnetic properties of hexagonal $BaFe_{12}O_{19}$ ferrite obtained by magnetic-field-assisted hydrothermal process. *Curr. Appl. Phys.* **2018**, *18*, 1426–1430.

54. Zlatkov, B.; Nikolić, M.; Aleksic, O.; Danninger, H.; Halwax, E. A study of magneto-crystalline alignment in sintered barium hexaferrite fabricated by powder injection molding. *J. Magn. Magn. Mater.* **2009**, *321*, 330–335. [CrossRef]